A dual quasi-zero-stiffness sliding-mode triboelectric nanogenerator for harvesting ultralow-low frequency vibration energy

Kai Wang [a,b], Jiaxi Zhou*[a,b], Huajiang Ouyang [c], Yaopeng Chang [a,b], Daolin Xu [a,b]

[a] *State Key Laboratory of Advanced Design and Manufacturing for Vehicle Body, Hunan University, Changsha 410082, PR China,*

[b] *College of Mechanical and Vehicle Engineering, Hunan University, Changsha 410082, PR China,*

[c] *School of Engineering, University of Liverpool, Liverpool L69 3GH, UK*

Abstract

A major purpose of energy harvesting from ambient vibration is to power sensors for structural health monitoring and environment monitoring. However, most types of ambient vibration are in the low-frequency region, which would make conventional energy harvesters inefficient. In this paper, the first attempt to combine a quasi-zero-stiffness (QZS) mechanism and a triboelectric nanogenerator is made, and a QZS triboelectric nanogenerator (QZS-TENG) is devised. In this QZS system, a negative stiffness mechanism (NSM) is constructed by using QZS springs to achieve ultra-low stiffness in a much larger displacement region than that of a traditional QZS device. Based on the geometrical relationship, the exact expression of the restoring force of the QZS-TENG is derived firstly, and then is fitted as a polynomial to obtain its approximate analytical dynamic responses. The electrical properties of the QZS-TENG, including its open circuit voltage, short circuit current, output voltage, output current and output power, are presented in both analytical and numerical results. The numerical results show excellent agreement with the analytical ones, and most importantly, the QZS-TENG exhibits an excellent energy harvesting performance in the ultralow frequency region. This work provides a new application of a QZS mechanism to harvest the ultralow-frequency vibration energy by combining a TENG.

* Corresponding author. College of Mechanical and Vehicle Engineering, Hunan University, Changsha 410082, PR China.
E-mail address: jxizhou@hnu.edu.cn (Jiaxi Zhou).

***Keywords*:** triboelectric nanogenerator; quasi-zero-stiffness; ultralow-frequency vibration energy; energy harvesting

1. Introduction

In general, it is hard to continuously power micro electric devices, sensors and wireless telecommunication systems. However, all of these devices mentioned above are important in structural health monitoring and environment monitoring. Therefore, designing an energy harvester to satisfy the needs of electric energy completely or partially by harvesting energy from the environment is a very attractive solution. In fact, the ambient energy, such as in airflow, water wave (river and ocean), mechanical and human motions, is abundant and exploitable. For example, ocean wave energy is estimated at around 1 TW [1]. The essential challenge of energy harvesting is how to convert ambient energy to electrical energy efficiently.

Fundamentally, principles to harvest energy from ambient vibration can be roughly categorized into four mechanisms [2]: electromagnetic mechanism [3–7], magnetoelectric mechanism [8], electrostatic mechanism [9] and piezoelectric mechanism [10–14]. An electromagnetic energy harvester converts mechanical energy of the ambient vibration to electrical energy when there is a relative motion between a magnetized body and a conductive coil. Compared with other energy harvesting mechanisms, an electromagnetic energy harvester is much simpler in structure, and it produces a higher output current and a lower output voltage. In addition, the electromagnetic field plays a vital role in ameliorating the energy harvesting performance of electromagnetic energy harvesters [15]. In contrast, a piezoelectric energy harvester exhibits a higher output voltage and lower output current, when the piezoelectric materials is subject to mechanical stress or strain. A magnetostrictive energy harvester generates electricity when magnetostrictive materials or metglas experience strain arising from a change of the magnetic field. Its energy harvesting performance is affected by the electromagnetic field obviously. In addition, engineering an energy harvester based on the dielectric electroactive polymer is also an alternative approach to convert the mechanical energy to electrical energy [16,17].

Compared with these three types of energy harvesters mentioned above, an electrostatic energy

harvester has a much simpler configuration. From the view of contact modes, there are five modes of the electrostatic energy harvester that can generate electricity [15,18,19], i.e. vertical contact mode [20–25], lateral sliding mode [26–30], freestanding triboelectric mode [29,31,32], bending friction mode [15,33] and single electrode mode [27,34,35]. Like a piezoelectric energy harvester, an electrostatic energy harvester also exhibits a high output voltage and a low output current. However, compared with a piezoelectric energy harvester, an electrostatic energy harvester produces an even greater output voltage. In order to improve the efficiency of the electrostatic energy harvester, Fan et al. [33] proposed a simple and low-cost triboelectric nanogenerator (TENG) based on the electrostatic mechanism, which provided an excellent way to harvest low-frequency ambient energy at high efficiency. Since then, various types of TENG have been proposed [18].

To harvest random vibrational energy in multiple directions over a wide bandwidth, a three-dimensional triboelectric nanogenerator was designed, analysed and tested experimentally [36]. In addition, introducing a mechanical spring-based amplifier and coupling two picking-up vibration structures, two types of TENGs were engineered to improve the vibration energy harvesting efficiency in the low-frequency region [37,38]. Niu et al. [27] proposed a theoretical model and derived an analytical relationship for a lateral sliding-mode triboelectric nanogenerator. Based on such a theoretical model, Salauddin et al. [39] proposed a hybrid energy harvester to harvest human-induced vibration energy. Yand et al. [40] also proposed a sliding-mode triboelectric nanogenerator, which was utilized to power a sensor that could detect the speed along one direction.

In fact, whatever the energy conversion mechanisms, electromagnetic energy harvesters, magnetoelectric harvesters or piezoelectric energy harvesters all fail to harvest vibration energy in a very low frequency region, since it is difficult to design an energy harvester with an ultralow resonant frequency [15]. The recent work [41–44] about negative stiffness mechanisms (NSMs), were capable of providing very low and even zero stiffness, called quasi-zero-stiffness (QZS) systems, and afford an opportunity for harvesting vibration energy at very low frequencies. In this paper, a novel QZS triboelectric nanogenerator (QZS-TENG) is put forward which combines a sliding-mode TENG and the QZS mechanism. In the QZS-TENG, four QZS springs are present and act as the negative stiffness mechanism, which can realise ultralow stiffness in a much larger displacement region than traditional QZS mechanisms. Since the proposed QZS-TENG has an ultralow resonant frequency, large-

displacement and -velocity responses in the very low-frequency region would appear, which is beneficial for collecting ultra-low frequency vibration energy.

2. Conception, modelling and analysis

2.1 Fundamental principle of QZS mechanism

Generally, energy harvesting performance depends upon the vibration response of the energy harvester. When system parameters remain unchanged, the greater the vibration response is, the higher amount of energy harvested is. Therefore, designing an energy harvester with a low resonant frequency is a main way to improve energy harvesting performance in low-frequency region. Introducing a NSM into a linear system to neutralize the stiffness of a linear spring is a promising approach to devise a QZS system with low resonant frequency. The comparisons of static and dynamics characteristics between a linear mass-spring system and a corresponding typical QZS system are illustrated in Fig. 1. It is clear that the stiffness of the QZS system is much lower than that of the linear system. Because of the lower stiffness feature, the vibration response amplitude in the ultra-low frequency region of the QZS system is larger than that of the linear system.

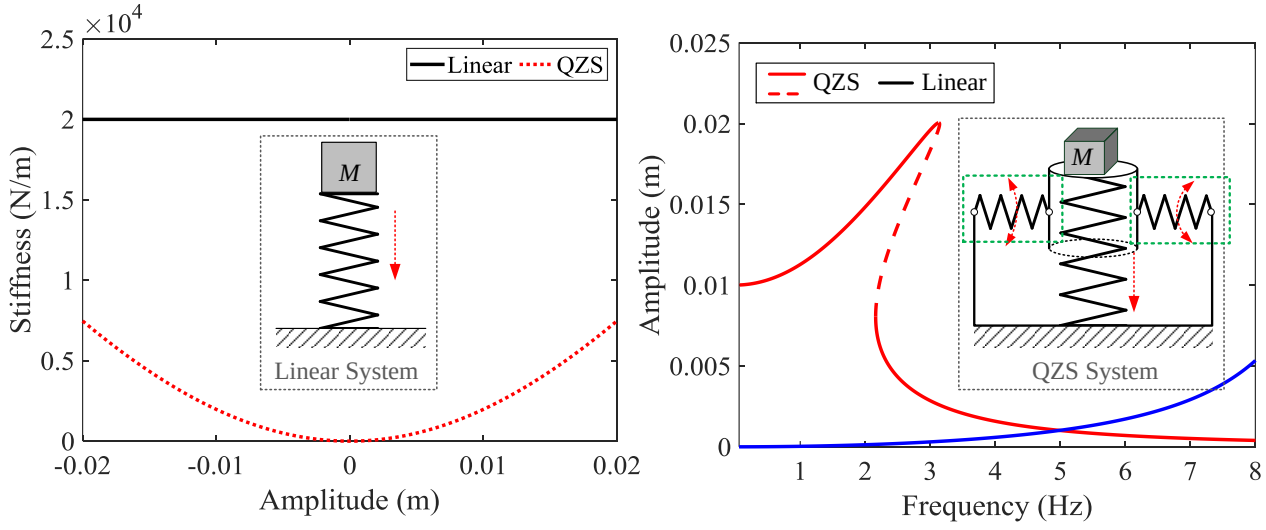

Fig. 1. (a) Stiffness characteristics and (b) dynamical characteristics for both the linear system ('Linear') and the conventional QZS system ('QZS').

2.2 QZS spring design in the dual QZS mechanism

The stiffness of the QZS system is equal to zero at the equilibrium position and close to zero in a displacement region near the equilibrium point. However, with the increase of the displacement, the stiffness of the QZS system increases rapidly, due to the neutralization of the NSM becomes less efficient. More importantly, such a variation of stiffness is detrimental to attainment of large-amplitude responses as well as high energy yield in the ultralow frequency region. In previous work, an analogous QZS structure was introduced into a QZS isolator to replace the traditional NSM. Since the reinforcement of the neutralization, the low stiffness region was broadened obviously[45]. Such an attempt is very beneficial to improve the ultralow frequency vibration isolation performance. However, it is only a tentative work to overcome the drawback of the conventional QZS system, and its configuration is relatively large, causing a difficulty in engineering application.

To devise a compact QZS structure with a large low-stiffness region, a magnetic-based QZS spring is proposed to replace the traditional NSM, i.e. inclined springs (enclosed by green dotted lines in Fig. 1), which is expected to enhance the neutralization of the NSM and broaden the low-stiffness region. The schematic diagram of the QZS spring is illustrated in Fig. 2, where the green part (2) and the blue part (3) denote the outer and inner magnet rings, respectively. Two sliding bearings are installed in the QZS spring to reduce the friction of the rod (4). Since the inner and outer permanent magnets are magnetized radially with opposite directions, the stiffness of the axial spring (5) could be neutralized by the pair of magnetic rings effectively.

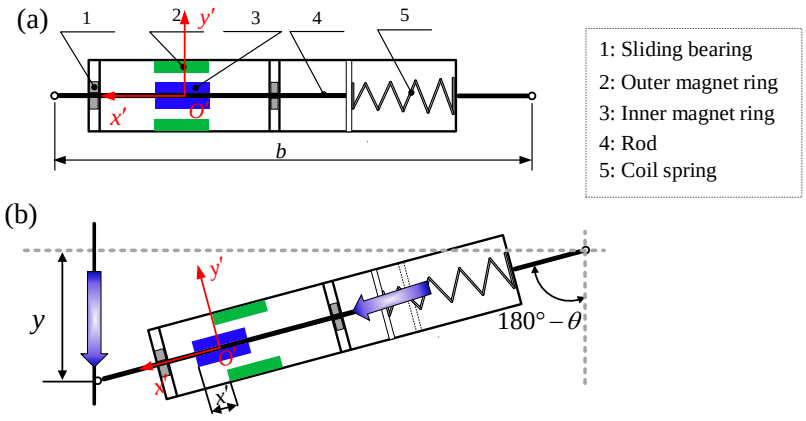

Fig. 2. Schematic diagram of the QZS spring. (a) Equilibrium position, (b) deformed configuration with a rotation angle of θ about the hinge point when an excitation applied on the QZS-TENG.

As shown in Fig. 2a, at the equilibrium position, the outer magnet ring and the inner magnet ring

are aligned with each other, and the axial spring is compressed. When an excitation applied on the QZS-TENG, the QZS spring will rotate around the hinge point with an angle of θ. In addition, the inner magnet ring departures from the equilibrium position by distance x, resulting in a thrust force along the axial direction. Thus, the QZS spring provides negative stiffness for the QZS-TENG along the vertical direction.

2.3 TENG design based on dual QZS mechanism

The schematic diagram of the QZS-TENG is shown in Fig. 3a and the corresponding computational model is shown in Fig. 3b. One end of the QZS spring is hinged onto the platform supported by the vertical spring, while the other end is fixed onto the cylindrical shell. The axial spring in the QZS spring is compressed and the top platform (or payload in practise) is supported totally by the vertical spring at the equilibrium position, which ensures a large carrying capacity of the QZS-TENG. The stiffness of the vertical spring can be substantially and even totally neutralized by the four QZS springs. Under the platform, a sleeve with four bonded glasses is fixed on the frame of the QZS-TENG. Four metal electrodes with a thickness of 0.01 mm are bonded with four dielectrics with length 40 mm and thickness 0.22 mm. Both the metal electrode and the dielectric are bonded on the glass. Moreover, four similar configurations are fixed onto the platform to form a sliding-mode triboelectric nanogenerator.

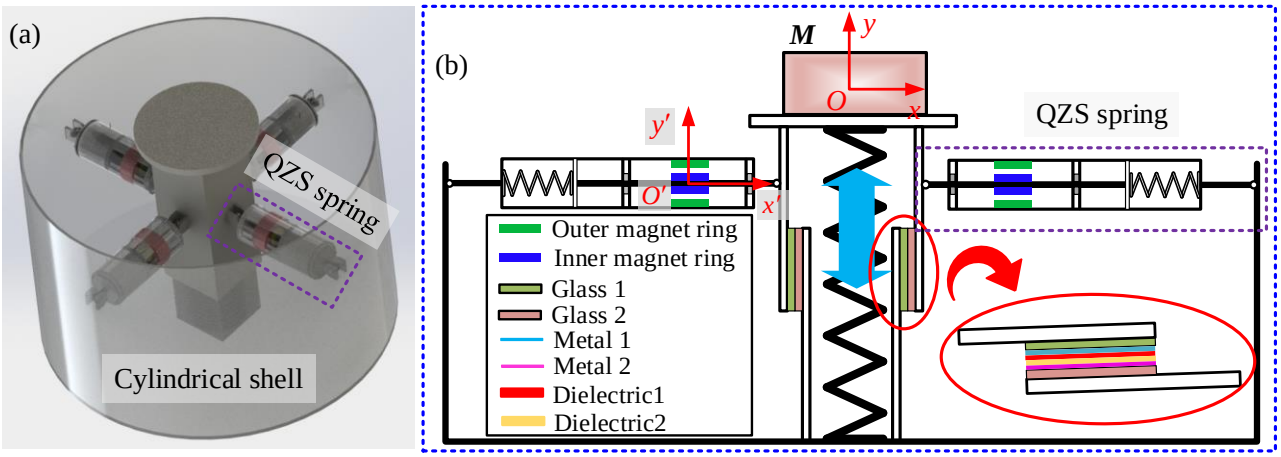

Fig. 3. Schematic diagram and computational model of the QZS-TENG. Symbols "Metal 1" and "Metal 2" represent metal electrodes.

Figure 3(b) presents the equilibrium position where the top platform mass (M) of the QZS-TENG

is supported by the vertical spring completely. Fig. 4 shows the fundamental principle of the QZS-TENG in one cycle of motion, where the blue points denote locations of Dielectric 1 and the platform. At the beginning of one cycle, the QZS-TENG locates at the static equilibrium position (as shown in Fig. 4-I) and two Dielectrics fully contact with each other. Due to the different ability of attracting electrons, Dielectric 1 loses electrons and exhibits a net positive charge on its surface. Dielectric 2 absorbs electrons lost from the surface of Dielectric 1, and forms a net negative charge on the surface of Dielectric 2. Both the negative and positive charges only spread on their surfaces, and the distance between Dielectric 1 and Dielectric 2 is so small that it can be neglected. Therefore, there is a small electric potential drop between two electrodes (Meta1 and Meta 2 in Fig. 3(b)) [46].

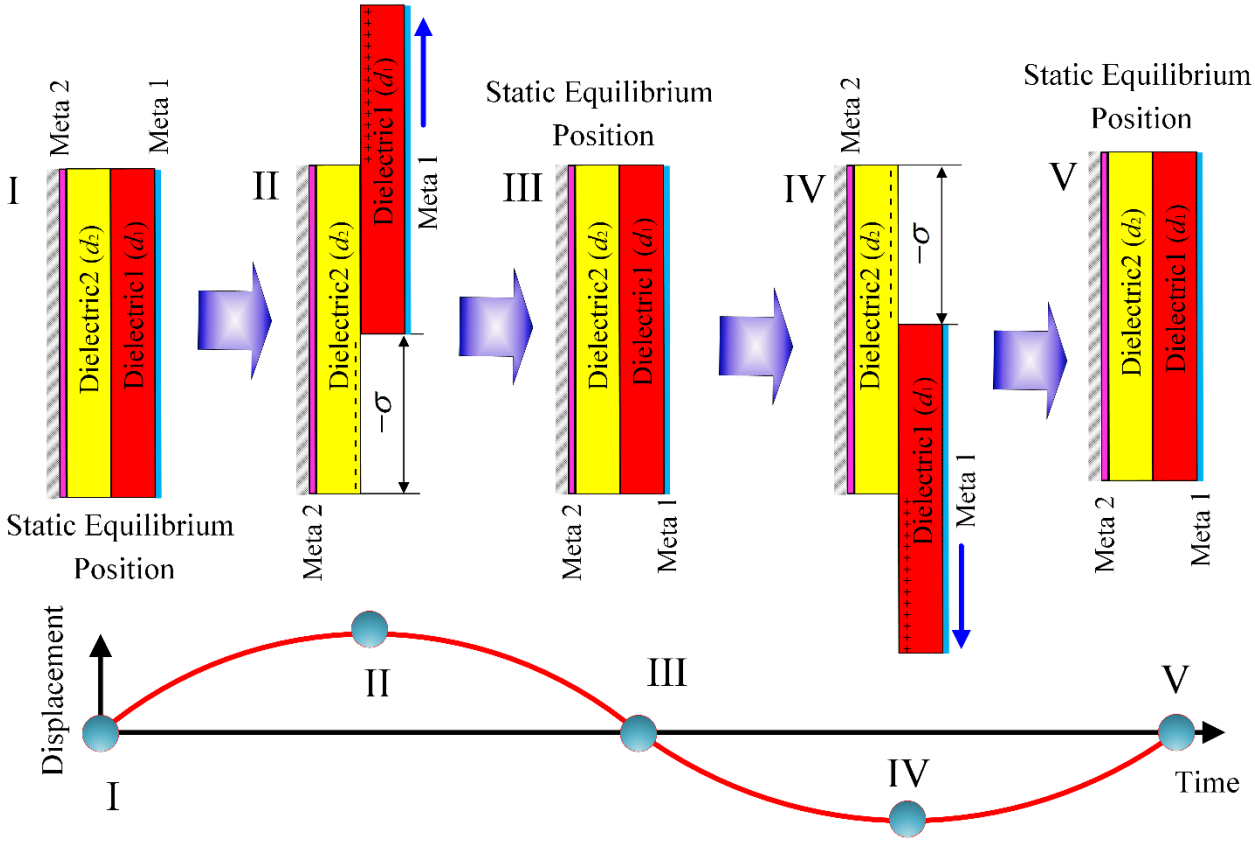

Fig.4. Operating principle of the QZS-TENG within one cycle of motion.

Once a vertical excitation acts on the QZS-TENG (Fig. 4-II), the top platform deviates from the static equilibrium position with a distance y and the QZS spring rotates around the hinge join with an angle of θ. The relative motion between the top platform and the base causes friction sliding between Dielectric 1 and Dielectric 2, resulting in instability of the charge distribution (with a surface density of tribo-charges σ in Dielectric 2 and $-\sigma$ in Dielectric 2). Then, an electric field is generated, which drives a current flow from the left electrode to the right electrode to cancel the tribo-charge-

induced potential [46].

When the platform reaches the maximum displacement (less than 0.9l [27]), the velocity between the platform and the base achieves a minimum value while the open circuit voltage peaks at a maximum value. After reaching the maximum upward displacement position (Fig. 4-II), Dielectric 1 moves downward, goes back to the static equilibrium position (Fig. 4-III) and reaches the maximum downward displacement position (Fig. 4-IV). Then, Dielectric 1 moves upward and returns to the static equilibrium position again (Fig. 4-V). Note that, the triboelectric mechanism of the QZS-TENG in the positive direction (upward in this paper) is appropriate to the separation of Dielectric 1 in the opposite direction. For brevity, the motion of Dielectric 1 from the static equilibrium position to the maximum downward position is not shown here.

2.4 Static analysis of dual QZS-TENG

As shown in Fig. 2, when the inner magnetic ring deviates from the static equilibrium position with a distance of x' (in the local-coordinate system), the magnetic force between the inner and the outer magnetic rings can be given by [47]

$$f_{\mathrm{M}}(x)=\frac{\sigma_1^2 R_m}{\mu_0}\left[2\phi(x')-\phi(x'+h)-\phi(x'-h)\right] \tag{1}$$

where $\sigma_1=\mathbf{J}\cdot\mathbf{n}$ denotes the magnetic pole surface density, $\mathbf{J}$ is the magnetic polarization vector and $\mathbf{n}$ is the unit normal vector. μ_0 is the permeability vacuum, and h the thickness of both inner and outer magnet rings. $R_m=R^*+l+g/2$ in which R^* is the inner radius of the inner permanent magnet, g the air gap between the inner and outer magnet rings and l the width of both the inner and outer magnet rings. The function ϕ is

$$\begin{aligned}\phi(a)=&(2l+g)\arctan\left(\frac{2l+g}{a}\right)-2(l+g)\arctan\frac{l+g}{a}+g\arctan\frac{g}{a}\\&-\frac{a}{2}\left\{\ln\left[(2l+g)^2+a^2\right]-2\ln(l+g)^2+\ln\left(g^2+a^2\right)\right\}\end{aligned} \tag{2}$$

The restoring force of the QZS spring can be written as

$$f_{\mathrm{S}}=kx'-f_{\mathrm{M}}(x') \tag{3}$$

where k denotes the stiffness of the horizontal spring in the QZS spring. Differentiating the expression

of the restoring force with respect to the local coordinate x', the stiffness of the QZS spring can be given by

$$k_{\mathrm{S}} = k - \frac{\sigma_1^2 R_m}{\mu_0}\left[2\varphi(x') - \varphi(x'+h) - \varphi(x'-h)\right] \tag{4}$$

where

$$\varphi(a) = -\frac{2a^2}{a^2 + (l+g)^2} - \frac{1}{2}\ln\frac{\left[(2l+g)^2 + a^2\right]\left(g^2 + a^2\right)}{(l+g)^4} \tag{5}$$

At the static equilibrium position $(x'=0)$, letting the stiffness of the QZS spring to be zero, a unique QZS condition for the parameters of the QZS spring can be given by

$$k_{\mathrm{QZS}} = \frac{\sigma_1^2 R_m}{\mu_0}\left\{\frac{4h^2}{h^2 + (l+g)^2} + \ln\frac{\left[(2l+g)^2 + h^2\right]\left(g^2 + h^2\right)}{(2l+g)^2 g^2}\right\} \tag{6}$$

where k_{QZS} denotes the optimal stiffness of the horizontal spring in the QZS spring, which ensures the stiffness of the QZS spring to equal zero at the equilibrium position. Substituting Eq. (6) into Eq. (3) and Eq. (4), the expressions of the restoring force and stiffness of the QZS spring can be given by

$$f_{\mathrm{SQZS}} = k_{\mathrm{QZS}}x' - \frac{\sigma_1^2 R_m}{\mu_0}\left[2\phi(x') - \phi(x'+h) - \phi(x'-h)\right] \tag{7}$$

$$k_{\mathrm{SQZS}} = k_{\mathrm{QZS}} - \frac{\sigma_1^2 R_m}{\mu_0}\left[2\varphi(x') - \varphi(x'+h) - \varphi(x'-h)\right] \tag{8}$$

Considering an external force applied on the QZS-TENG, according to the geometric relationship shown in Fig. 3(a) and introducing a parameter ψ^* to denote the compression of the linear spring of the QZS spring, the restoring force of the QZS-TENG can be written as

$$F = Ky - 4\tilde{f}_{\mathrm{SQZS}}\sin\theta \tag{9}$$

where K denotes the stiffness of the vertical spring, and y is the displacement of the platform. θ denotes the angle of the QZS spring rotated around the hinge point. It should be noted that $\tilde{f}_{\mathrm{SQZS}}$ is not equal to f_{SQZS}, since once an excitation is applied on the QZS-TENG, the QZS spring provides a thrust force along the vertical direction. Introducing a parameter γ (named as stiffness ratio in the

following text) to denote the ratio of the stiffness of the NSM at the static equilibrium position to the stiffness of the horizontal spring, the restoring force of the QZS spring can be written as

$$\tilde{f}_{\mathrm{SQZS}} = \gamma k_{\mathrm{QZS}}\left(\psi^{*} - x'\right) + \frac{\sigma_1^2 R_m}{\mu_0}\left[2\phi\left(x'\right) - \phi\left(x'+h\right) - \phi\left(x'-h\right)\right] \tag{10}$$

Substituting $\sin\theta = y/\sqrt{y^2+b^2}$ and Eq. (10) into Eq. (9), the restoring force of the QZS-TENG can be rewritten as

$$F_{\mathrm{EH}} = Ky - \frac{4y\left\{\gamma k_{\mathrm{QZS}}\left(\psi^{*} - x'\right) + \frac{\sigma_1^2 R_m}{\mu_0}\left[2\phi\left(x'\right) - \phi\left(x'+h\right) - \phi\left(x'-h\right)\right]\right\}}{\sqrt{y^2+b^2}} \tag{11}$$

where b is the length of the QZS spring at the static equilibrium position. According to the geometrical relationship of the QZS-TENG, the local coordinate $\left(x'\right)$ of the QZS spring can be expressed with respect to the displacement of the QZS-TENG

$$x' = \sqrt{b^2+y^2} - b \tag{12}$$

Substituting Eq. (12) into Eq. (11) and differentiating Eq. (11) with respect to the vertical displacement y, the stiffness of the QZS-TENG can be given by

$$K_{\mathrm{EH}} = K - 4\gamma k_{\mathrm{QZS}}\left[\frac{b^2\left(\psi^{*} - \sqrt{b^2+y^2} + b\right)}{\left(b^2+y^2\right)^{\frac{3}{2}}} - \frac{y^2}{b^2+y^2}\right] - p_1 - p_2 \tag{13}$$

where

$$p_1 = \frac{4\sigma_1^2 R_m b^2}{\mu_0\left(y^2+b^2\right)^{\frac{3}{2}}}\left[2\phi\left(\sqrt{b^2+y^2}-b\right) - \phi\left(\sqrt{b^2+y^2}-b+h\right) - \left(\sqrt{b^2+y^2}-b-h\right)\right] \tag{14}$$

$$p_2 = \frac{4y^2\sigma_1^2 R_m}{\mu_0\left(y^2+b^2\right)}\left[2\varphi\left(\sqrt{b^2+y^2}-b\right) - \varphi\left(\sqrt{b^2+y^2}-b+h\right) - \varphi\left(\sqrt{b^2+y^2}-b-h\right)\right] \tag{15}$$

At the static equilibrium position $\left(y=0\right)$, letting the stiffness of the QZS-TENG to be zero, a QZS condition for the QZS-TENG can be derived and written as $\gamma k_{\mathrm{QZS}}/\mathrm{K} = b/4\psi^{*}$. Substituting such a condition into Eq. (11) and Eq. (13), the expressions of both the restoring force and stiffness of the QZS-TENG can be rewritten as

$$F_{\mathrm{EH,QZS}} = K\left[y - \frac{by\left(\psi^* - x\right)}{\psi^*\sqrt{y^2+b^2}} \right] - \frac{4\sigma_1^2 R_m y}{\mu_0\sqrt{y^2+b^2}}\left[2\phi\left(x'\right) - \phi\left(x'+h\right) - \phi\left(x'-h\right)\right] \tag{16}$$

$$K_{\mathrm{EH,QZS}} = K\left\{1 - \frac{b}{\psi^*}\left[\frac{b^2\left(\psi^* - \sqrt{b^2+y^2}+b\right)}{\left(b^2+y^2\right)^{\frac{3}{2}}} + \frac{y^2}{b^2+y^2}\right]\right\} - p_1 - p_2 \tag{17}$$

Obviously, given a displacement, one can easily obtain the restoring force and stiffness of the QZS-TENG according to Eq. (16) and Eq. (17).

2.5 Static features of dual QZS-TENG

Based on the static analysis and the geometrical parameters tabulated in Table 1, the effect of the parameter γ on the stiffness feature of the QZS TENG is presented in Fig. 5. In this figure, black and white lines denote the stiffness of the QZS-TENG ranging from 1000 N/m to 0 N/m, respectively. Clearly, a threshold value of the parameter $\left(\gamma = 0.77\right)$ can be found at the intersection of the white lines, which corresponds to the largest displacement region (thus having the lowest stiffness). In addition, as highlighted by the purple solid line in Fig. 5, the stiffness value of 1000 N/m is designed as the critical value for defining the displacement region of low stiffness.

Table 1
Fundamental structure parameters of the QZS-TENG

Parameter	Value
Magnetic pole surface density σ_1	1 T
Permeability of the vacuum μ_0	$4\pi\times10^{-7}$ N/A
Inner radius of the inner permanent magnet R^*	2 mm
Width of both the inner and outer permanent magnets *l*	4 mm
Thickness of both the inner and outer permanent magnets *h*	5 mm
Air gap between the inner and outer permanent magnets *g*	2 mm
Length of the QZS spring at the rest equilibrium position *b*	80 mm
Stiffness of the vertical spring *K*	2×10^4 N/m
Optimal stiffness of the horizontal spring in the QZS spring k_{QZS}	1.65×10^4 N/m

Mass of the platform M	5 kg

Moreover, the low stiffness displacement region decreases with the increase of the parameter γ from 0.77 to 1 and reaches the minimum one when $\gamma = 1$. It should be noted that the stiffness of the QZS-TENG is negative in some displacement regions when $\gamma < 0.77$, which would make the QZS-TENG unstable and is not considered here. In a special case of Fig. 5(a), the stiffness-displacement curve for the threshold value is presented in Fig. 5(b). Clearly, the stiffness of the QZS-TENG is equal to zero at the static equilibrium position, and close to zero in a large displacement region around the equilibrium position. Compared with a conventional QZS system presented in Fig. 1, the stiffness-displacement curve is more flat, and the displacement region of low stiffness is wider, which is instrumental in producing a large dynamic response at low frequencies of excitation and then convert the mechanical energy to electric energy efficiently. Therefore, the threshold value $(\gamma = 0.77)$ is utilized in the following theoretical analysis.

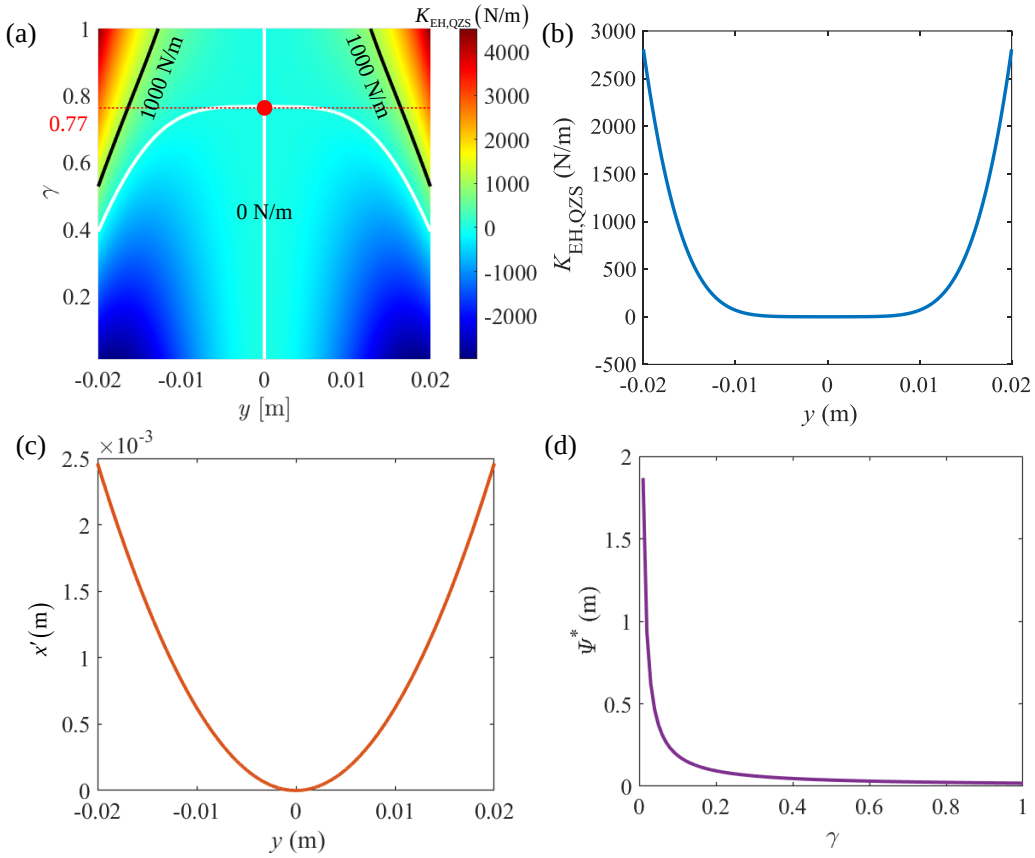

Fig. 5. (a) The effect of the parameter γ on the stiffness. (b) Stiffness of the QZS-TENG when $\gamma = 0.77$. (c) The relationship between the local coordinate x' and the vertical displacement y. (d) The influence of the parameter

γ on the compression Ψ^*.

The relationship between vertical displacement y and local coordinate x' is depicted in Fig. 5(c). Clearly, the displacement of the QZS spring is smaller than that of the QZS-TENG. Fig. 5(d) illustrates the effect of the parameter γ on the compression of the linear spring within the QZS spring. From this figure, one can find that a large contraction is needed at the static equilibrium position to achieve the QZS function if the parameter γ is small. Since the limitation of the geometrical configuration, it is hard to devise a small size QZS-TENG for harvesting mechanical energy from the ultra-low frequency ambient vibration. With the increase of γ, the contraction of the horizontal linear spring decreases rapidly, which provides an opportunity to design a compact QZS-TENG.

To analyse the QZS-TENG from an analytical view, the complicated expression of the restoring force is fitted as a polynomial with components of y, y^3, y^5 and y^7 based on the trust-region-reflective algorithm. The expressions of the dimensionless restoring force and stiffness of the QZS-TENG are given by

$$\bar{K}^{\mathrm{c}}_{\mathrm{EH,QZS}} = a_c + 3a_1\bar{y}^2 + 5a_2\bar{y}^4 + 7a_3\bar{y}^6 \tag{18}$$

$$\bar{F}^{\mathrm{c}}_{\mathrm{EH,QZS}} = a_c\bar{y} + a_1\bar{y}^3 + a_2\bar{y}^5 + a_3\bar{y}^7 \tag{19}$$

where $a_c = 0.006$, $a_1 = -0.45$, $a_2 = 14.74$ and $a_3 = -27.69$ in this particular design. The fitted expression will be utilized to carry out the analytical dynamic analysis of the QZS-TENG in the following Section 3.

3. Dynamic analysis of the QZS-TENG

3.1 Analytical solutions

Considering an excitation with amplitude F and driving frequency ω applied on the QZS-TENG, the equation of motion of the system can be given by

$$M\ddot{y} + c\dot{y} + F_{\mathrm{EH,QZS}} = F\cos(\omega t + \varphi) \tag{20}$$

where M is the top platform mass of the QZS-TENG, and $F_{\mathrm{EH,QZS}}$ is the restoring force. The

electrostatic force between the two dielectric films can be given by

$$F_{\mathrm{e}}=\frac{Q^{2}}{2\varepsilon_{0}\varepsilon_{\mathrm{r}}A} \tag{21}$$

where A denotes the contact area between the two dielectric films. Actually, such an electrostatic force has an extremely low impact on the dynamic characteristics of the QZS-TENG according to the research work conducted by Fu et al. [30]. Therefore, the effect of the electrostatic force is neglected and only the friction is considered in this work. To simplify the analysis, the friction between the two dielectrics and the friction coming from the mechanical structure are simplified as a linear viscous damping with coefficient c in the dynamical model. Utilizing the following items, $\zeta=c/2\sqrt{MK}$, $\Omega=\omega/\omega_{0}$, $\bar{F}=F/Kb$, $\tau=\omega_{0}t$ and $\omega_{0}=\sqrt{K/M}$, the dimensionless equation of motion of the QZS-TENG can be given by

$$y''+2\zeta y'+\bar{F}_{\mathrm{EH,QZS}}^{\mathrm{c}}=\bar{F}\cos\left(\Omega\tau+\varphi\right) \tag{22}$$

Assuming the solution of the displacement response $y=Y\cos\left(\Omega\tau\right)$ and substituting it into the dimensionless equation of motion, one can obtain

$$-Y\Omega^{2}\cos\left(\Omega\tau\right)+2\zeta Y\Omega\sin\left(\Omega\tau\right)+\bar{F}_{\mathrm{EH,QZS}}^{\mathrm{c}}=\bar{F}\cos\left(\Omega\tau+\varphi\right) \tag{23}$$

By using trigonometry operations, Eq. (23) can be expanded as an expression containing the first-order harmonics and high-order harmonics. According to the Harmonic Balance method and neglecting higher-order harmonics, the amplitude-frequency equation can be derived

$$\left(-\Omega^{2}+a_{c}Y+\frac{3}{4}a_{1}Y^{3}+\frac{5}{8}a_{2}Y^{5}+\frac{35}{64}a_{3}Y^{7}\right)^{2}+\left(2\zeta\Omega Y\right)^{2}=\bar{F}^{2} \tag{24}$$

By solving Eq. (24), the relationship between the excitation frequency and the response amplitude can be written as

$$\Omega_{1,2}=\sqrt{\frac{\Gamma}{Y}-2\zeta^{2}\pm\frac{1}{Y}\sqrt{4\zeta^{4}Y^{2}-4\zeta^{2}\Gamma Y+\bar{F}^{2}}} \tag{25}$$

where Γ denotes a coefficient [45]. For the QZS-TENG, the open circuit voltage can be given by [27,39]

$$|V_{\mathrm{OC(TENG)}}|=\frac{\sigma y}{\varepsilon_0\left(L-y\right)}\left(\frac{d_1}{\varepsilon_1}+\frac{d_2}{\varepsilon_2}\right) \tag{26}$$

where y is the separation distance between two friction surfaces, d_1 and d_2 denote the thickness of Dielectric 1 and Dielectric 2, respectively. L denotes the length of the dielectric, σ is the charge density, ε_1 and ε_2 are the relative permittivity of Dielectric 1 and Dielectric 2, respectively. ε_0 is the permittivity of free space. In addition, the current flow in the QZS-TENG can be given by [28,39]

$$I_{\mathrm{sc(TENG)}}=\sigma w\frac{\mathrm{d}y}{\mathrm{d}t}=\sigma w v\left(t\right) \tag{27}$$

where w denotes the width of the dielectric and $v(t)$ is the sliding velocity between the dielectrics. By solving Eq. (25), one can obtain the displacement $y=Y\cos\left(\Omega\tau\right)$ and the velocity $\dot{y}=-\Omega Y\sin\left(\Omega\tau\right)$ of the QZS-TENG. By substituting the responses into Eq. (26) and Eq. (27), the open circuit voltage and the short circuit current can be rewritten as

$$V_{\mathrm{OC(TENG)}}=\frac{\sigma Y\cos\left(\omega t\right)}{\varepsilon_0\left[L-Y\cos\left(\omega t\right)\right]}\left(\frac{d_1}{\varepsilon_{r1}}+\frac{d_2}{\varepsilon_{r2}}\right) \tag{28}$$

$$I_{\mathrm{sc(TENG)}}=\sigma w\frac{\mathrm{d}y}{\mathrm{d}t}=-\sigma w\omega Y\sin\left(\omega t\right) \tag{29}$$

For a given excitation, one can easily obtain the response amplitude according to Eq. (24), as well as the open circuit voltage and the short circuit current according to Eq. (28) and Eq. (29), respectively.

3.2 Analytical results

Fig. 6 demonstrates the displacement amplitude of the QZS-TENG under different excitation amplitudes and different damping ratios. In this figure, black solid lines and red dotted lines represent the stable and unstable solutions of the displacement response, respectively. The blue points denote the jump-down frequency, and the jump-down phenomenon occurs when the excitation frequency exceeds such a point. From Fig. 6(a), it is clear that with the increase of the excitation amplitude, the displacement amplitude notably increases and the jump-down phenomenon becomes more evident. Fig. 6(b) shows the effect of the damping ratio on the displacement response. Clearly, with the decrease of the damping ratio, the displacement amplitude of the QZS-TENG also increases

significantly. According to reference [39], the damping ratio $\zeta = 0.022$ is elected for the following analyses.

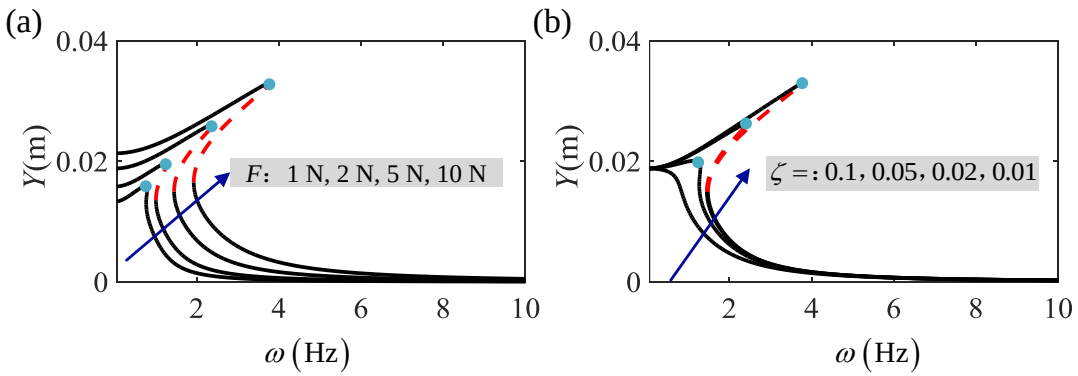

Fig. 6. Comparisons of the amplitude of the displacement response of the QZS-TENG under different (a) excitation amplitudes and (b) damping ratios.

Some parameters of the QZS-TENG are selected from reference [27]. All parameters related to the sliding-mode triboelectric nanogenerator are tabulated in Table 2. The effect of the excitation amplitude on the open circuit voltage and short current is reported in Fig.7. Clearly, with the increase of the excitation amplitude, both the open circuit and the short current increase. Thus, the QZS-TENG could be more efficient when the excitation amplitude is large. These analytical results provide a direct way to evaluate the effectiveness of the QZS-TENG.

Table 2. Electrical parameters of the QZS-TENG

Parameter	Value
Dielectric 1	$\varepsilon_{r1} = 4,\ d_1 = 2.2\times10^{-4}$ m
Dielectric 2	$\varepsilon_{r2} = 2,\ d_2 = 2.2\times10^{-2}$ m
Width of the Dielectrics	w=0.04 m
Length of the Dielectrics	L=0.04 m
Surface tribo-charge density [39]	$\sigma = 80\,\mu\text{C/m}^2$

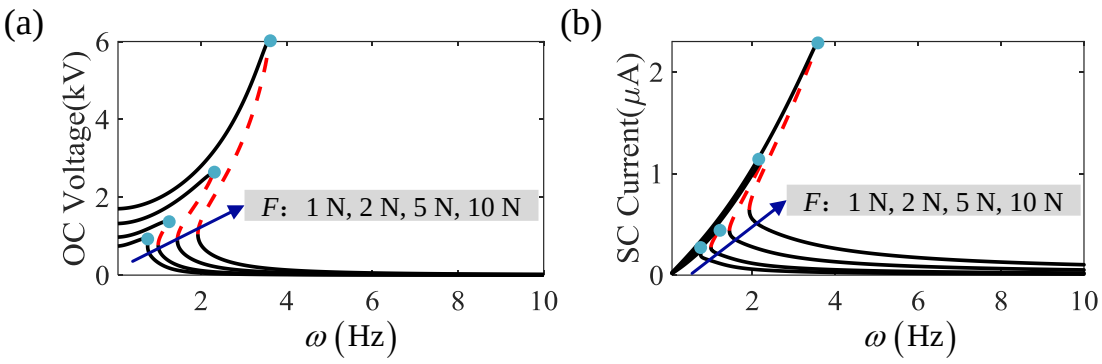

Fig. 7. Analytical results for (a) the open-circuit voltage and (b) the short-circuit current of the QZS-TENG for different excitation amplitudes.

4. Numerical simulations of the QZS-TENG

To verify the analytical results of the QZS-TENG and obtain the output voltage, the output current and the output power, the mechanical-electrical coupling equation is established using the exact expression of the restoring force. According to Niu. et al. [27], the approximate Voltage-Charges-Displacement relationship of the sliding-mode TENG is given by

$$V = -\frac{Q}{w\varepsilon_0 L(l-y)}\left(\frac{d_1}{\varepsilon_1}+\frac{d_2}{\varepsilon_2}\right)+\frac{\sigma y}{\varepsilon_0(L-y)}\left(\frac{d_1}{\varepsilon_1}+\frac{d_2}{\varepsilon_2}\right) \tag{30}$$

where Q denotes the total amount of transferred charges between electrodes. Considering a resistor R and according to Ohm's law, the relationship between the current and the voltage can be given by

$$V = IR = R\frac{\mathrm{d}Q}{\mathrm{d}t} \tag{31}$$

Substituting Eq. (30) into Eq. (31), one can obtain

$$R\frac{dQ}{dt} = -\frac{Q}{w\varepsilon_0(L-y)}\left(\frac{d_1}{\varepsilon_{r1}}+\frac{d_2}{\varepsilon_{r2}}\right)+\frac{\sigma y}{\varepsilon_0(L-y)}\left(\frac{d_1}{\varepsilon_{r1}}+\frac{d_2}{\varepsilon_{r2}}\right) \tag{32}$$

Combining the equation of motion, Eq. (20) , and the electrical equation, Eq. (32), and solving these mechanical-electrical coupling equation of the QZS-TENG through the Runge-Kutta method, one can obtain the output current and the output voltage of the QZS-TENG.

4.1 Verification of the analytical results

Fig. 8 reports time histories of the displacement response, the velocity response, the open circuit voltage and the short circuit current. Clearly, the response can be divided into two stages by the jump-down frequency. In the first stage, the excitation frequency is lower than the jump-down frequency, and both the displacement and velocity response amplitude, as well as the electrical response amplitude of the QZS-TENG increase with the driving frequency. When the driving frequency exceeds the jump-down frequency (3.55 Hz calculated by Eq.(25)), the response enters into the second stage, and the open circuit voltage and the short circuit current decrease suddenly. By comparing the analytical and numerical results, one can find excellent agreement. Therefore, the analytical method is capable of accurately predicting the dynamic response to evaluate the energy harvesting efficiency of the QZS-TENG.

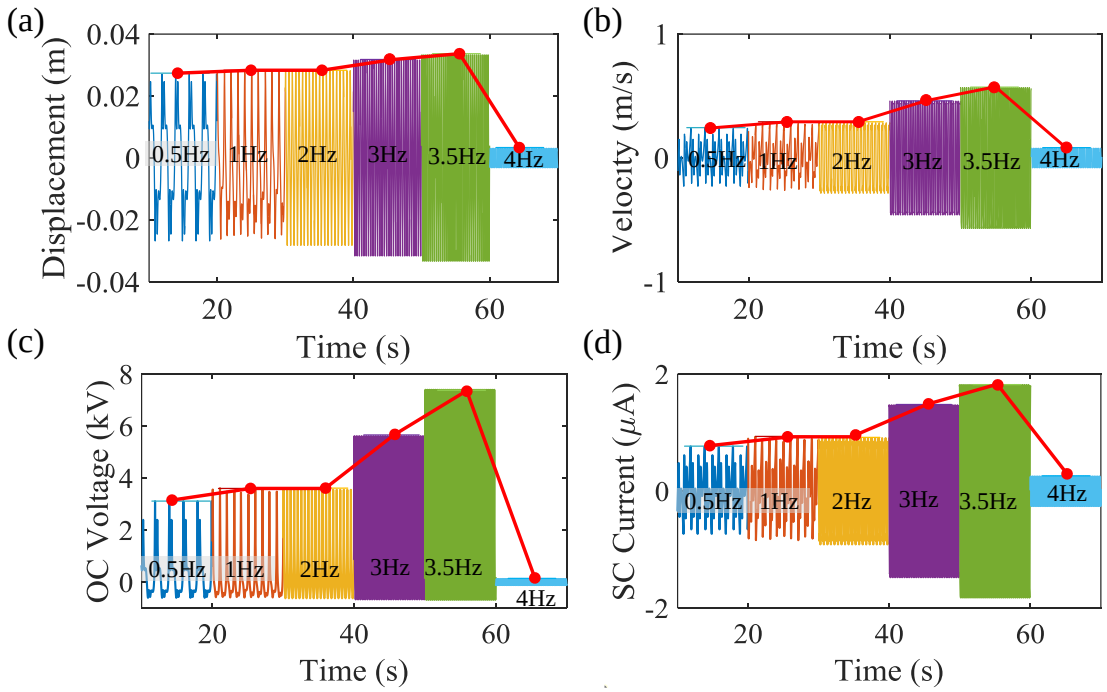

Fig. 8. The time histories of (a) displacement response, (b) velocity response, (c) the open-circuit voltage response and (d) the short-circuit current response of the QZS-TENG for different excitation frequencies. Red lines denote the trend lines.

4.2 Relevance between load resistance and output characteristics

The dependences of the output voltage, the output current and the output power on the load

resistance is shown in Fig. 9. The equivalent circuit model of the QZS-TENG with a load resistance is inserted into Fig. 9b. Clearly, the effect of the load resistance on the output characteristics can be divided into three working regions. In the first one, region I in Fig. 9, the load resistance is small, and as the load resistance increases, the output current keeps constant that is equal to the short-circuit current roughly. The output voltage also keeps unchanged and is close to zero in such a case. When the load resistance continues to increase and enters the second working region, the output current experiences a fast growth and then decreases dramatically as the increase of the load resistance. The increase of the output current in region II can be attributed to a fact that the increasing speed of the voltage peak value is greater than the increasing speed of the resistance [27]. In region III, the load resistance is sufficiently large and the output characteristics are close to these in the open-circuit condition. The output current is in close proximity to zero, and the voltage keeps a constant that equals to the open-circuit voltage.

As shown in Fig. 9b, the instantaneous power is almost 0 when the load resistance is in region I. With the increase of the load resistance (region II), the QZS-TENG reaches its maximum instantaneous output power of 6.05 mW. When the resistance exceeds that optimal one corresponding to the maximum output power, the instantaneous power decreases dramatically to a small value and then closes to zero again in region III. Therefore, the optimum load resistance can be determined from this figure to produce the maximum output power.

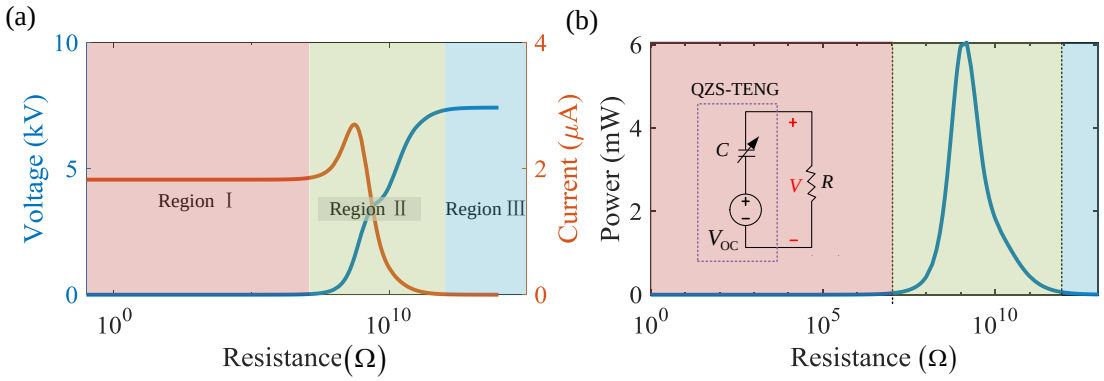

Fig. 9. Numerical results of the QZS-TENG. (a) The influence of the load resistance on the peak output current and voltage. (b) Maximum peak output power profile with the load resistance. The subplot in Fig. 9 (b) represents the equivalent circuit model of the QZS-TENG with a load resistance.

Based on the analysis conducted above, it is clear that the load resistance is a pivotal parameter

to achieve the best instantaneous power output. Actually, the variation of the output power can be interpreted by the impedance matching process between the inherent capacitance of the QZS-TENG and the load resistance [48]. For the case of small load resistance (region I in Fig. 9), the inherent condensance of the QZS-TENG is much larger than that of the load resistance. Hence, the total impedance of the QZS-TENG is mainly dependent on its inherent capacitance, which results in a nearly unchanged output current with the increase of the load resistance. On the other hand, when the resistance is in region III, the load resistance is quite large, and the total impedance of the QZS-TENG primarily determined by the load resistance. Therefore, the QZS-TENG is almost in an open-circuit condition and the output voltage keeps unchanged. In the third case, the load resistance belongs to region II, and the impedance of the QZS-TENG is affect by both the load resistance and the inherent capacitance. The output current in the circuit reduces while the voltage rises with the increase of the load resistance. When the load resistance matches the impedance determined by the inherent capacitance, the maximum instantaneous power output is achieved.

4.3 Effect of the stiffness ratio

The influences of the stiffness ratio on the instantaneous power output and the optimal load resistance are depicted in Fig. 10, when the excitation frequency is 3 Hz. Fig. 10b details the output power corresponding to the stiffness ratio. Clearly, with the increase of the stiffness ratio from 0.77 (the parametric condition for a dual QZS mechanism) to 1, the instantaneous power output decreases by about one half approximately from 4.06 mW to 2.37 mW. Actually, the variation of the output power resulted from the stiffness ratio can be interpreted by the mechanical changes of the QZS-TENG.

As discussed in section 2, the stiffness ratio plays a pivotal role in the realization of the QZS-TENG. When the stiffness ratio is equal to 0.77, the QZS-TENG is a dual QZS system that produces a flat stiffness-displacement curve in a large displacement region. Thus, the QZS-TENG could generate a response with large amplitude. With the increase of the stiffness ratio, the QZS-TENG approaches a conventional QZS system, and the displacement region for low stiffness reduces gradually. When the stiffness ratio increases to 1, the negative stiffness mechanism (magnet rings) in the QZS spring becomes unworkable, and only the axial spring provides negative stiffness along the

vertical direction. The QZS-TENG switches into a traditional QZS system, and its stiffness increases notably when it deviates from the equilibrium position. The decrease of the low-stiffness displacement region causes the decrease of the displacement amplitude and eventually leads to a reduction in efficiency of energy harvesting.

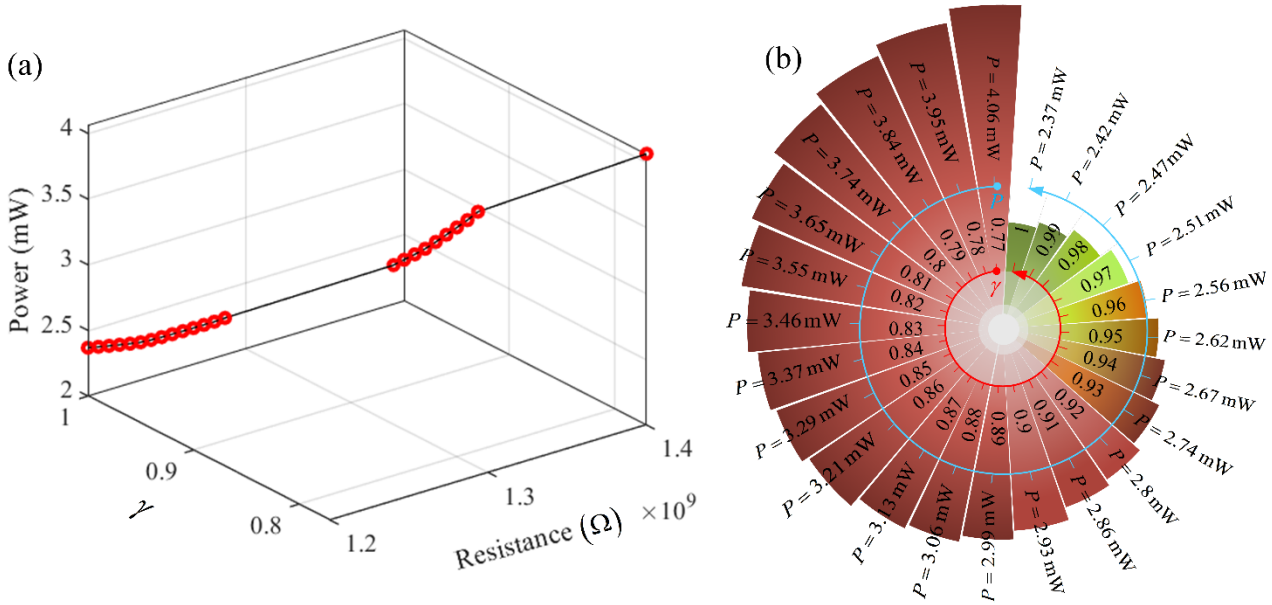

Fig.10. The effect of the stiffness ratio γ on the optimal load resistance and the instantaneous power output when the excitation frequency is 3 Hz. (a) The relationship between the output power and the parameter γ as well as the optimal load resistance. (b) The instantaneous power outputs of the QZS-TENG for different γ.

In addition, the optimal load resistance is also dependent on the stiffness ratio. According to the reference [27], the inherent capacitance of the QZS-TENG can be estimated by

$$C = \frac{\varepsilon_0 w(L-y)\varepsilon_{r1}\varepsilon_{r1}}{d_1\varepsilon_{r1} + d_2\varepsilon_{r1}} \tag{33}$$

The impedance of the QZS-TENG induced by its inherent capacitance can be given by $1/(\omega_{\text{QZS-TENG}}C)$, where $\omega_{\text{QZS-TENG}}$ denotes the frequency of V_{OC}. Clearly, with the increase of the displacement y, the capacitance decreases and the capacitive reactance increases. According to the impedance matching concept, the optimal load resistance increases with the increase of the response amplitude. When the stiffness ratio decreases from 1 to 0.77, therefore, the optimal load resistance increases.

4.4 Effect of the excitation amplitude

As elucidated in section 2, the stiffness of the QZS-TENG is nonlinear and related to the displacement of the platform. Therefore, the excitation amplitude has an obvious effect on the displacement and velocity responses, as well as the electrical characteristics. As depicted in Fig. 11, with the increase of the excitation amplitude, the output current, the output voltage and the output power rise simultaneously.

Note that, the increase of the electrical feature is not in a linear trend with respect to the increasing excitation amplitude. Specifically, when the force amplitude increases from 7 N to 8 N, there are sharp increases in the current, voltage and power. These can be attributed to a fact that the QZS-TENG is a nonlinear system and the jump-down phenomenon is related to the displacement amplitude. As shown in Fig. 6, as the excitation amplitude increases, the jump-down frequency keeps increasing gradually. In fact, the selected excitation frequency 3Hz would exceed the jump-down frequency of the QZS-TENG, when the excitation amplitude is small, such as 5 N. In this condition, the QZS-TENG generates quite small output power. When the amplitude increases further (>7 N), the jump-down frequency exceeds the selected excitation frequency, and the QZS-TENG oscillates with large amplitude, leading to outstanding electrical output.

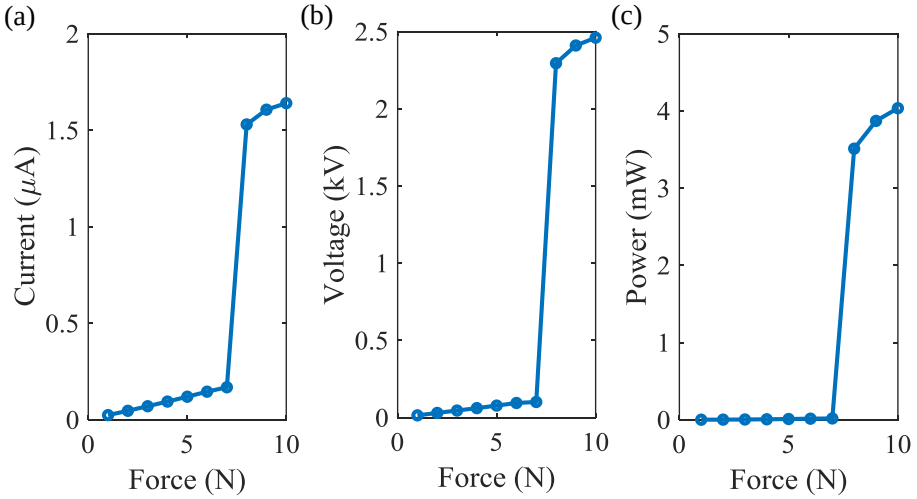

Fig. 11. The effect of the excitation amplitude on (a) the output current, (b) the output voltage and (c) the output power when the excitation frequency equals 3 Hz.

4.5 Effect of assembly error

In practical application, it is hard to fabricate an ideal prototype due to the manufacturing and assembling errors. More importantly, the errors could lead to a deviation of the equilibrium position and affect the dynamic responses obviously. Therefore, evaluating the effect of the errors on the energy harvester is quite important for its application.

When the actual mass of the top platform deviates from the designed one by a percentage of λ, namely, the top platform mass changes from M to $(1+\lambda)M$, the equation of motion of the QZS-TENG can be given by

$$M\ddot{y} + c\dot{y} + F_{\mathrm{EH,QZS}} = \gamma M\mathrm{g} + F\cos(\omega t + \varphi) \tag{34}$$

Note that, the increment of mass γM is regarded as a case of assembling error and leads the QZS-TENG to reach a new equilibrium position. Fig. 12 shows the dynamics responses of the QZS-TENG with different platform mass. The red solid line with two circles denotes the results calculated by a forward frequency sweeping from 5 Hz to 0.1 Hz. The blue solid line with two circles is the peak-to-peak value of the displacement of the QZS-TENG obtained through a backward frequency sweeping from 0.1 Hz to 5 Hz.

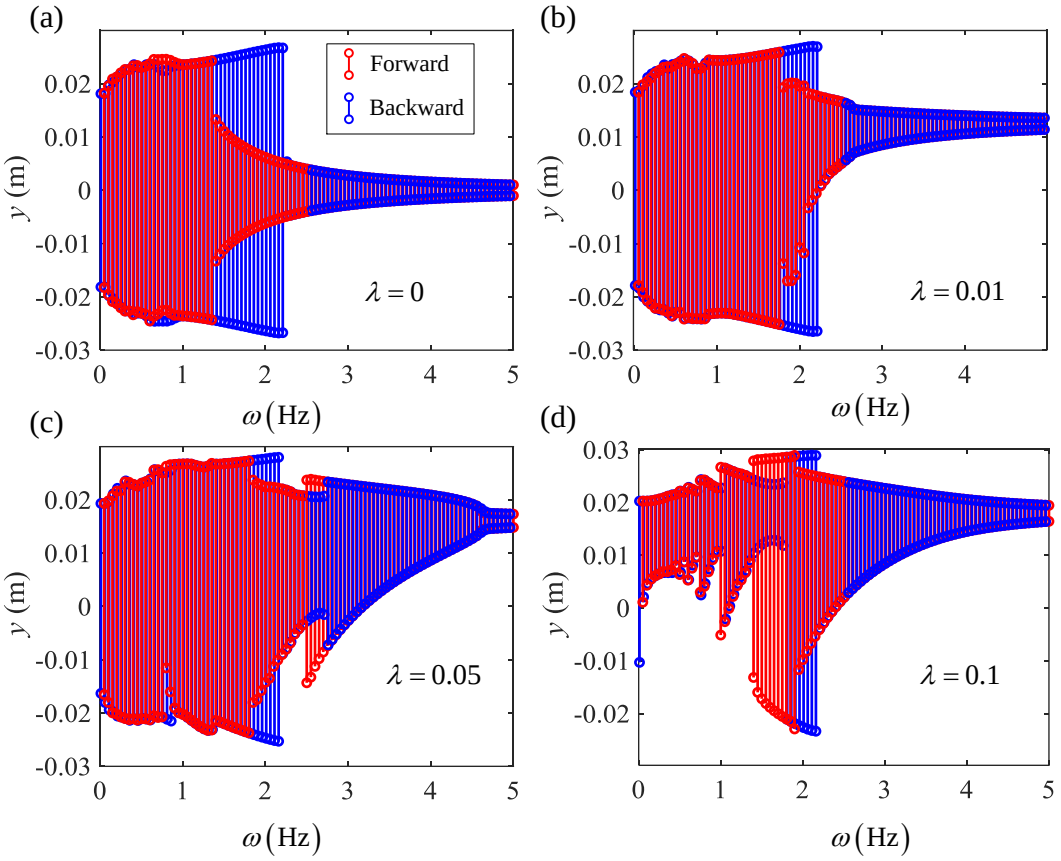

Fig. 12. Influence of the mismatch of the designed mass on the dynamic response (peak-peak) of the QZS-TENG when the excitation amplitude equals 5N.

As shown in Fig. 12, it is evident that with the increase of λ from 0 to 0.05, the peak-to-peak displacement response of the QZS-TENG in the low frequency range (<2.2 Hz) shows little variation. When the excitation frequency exceeds the jump-down frequency (~2.2 Hz), the QZS-TENG oscillates at one side of the designed equilibrium position. However, when λ increases to 0.1, the QZS-TENG oscillates at the actual equilibrium position with a low peak-to-peak value in the low frequency range. Once the excitation frequency approaches to the resonant frequency, the resonant response of the QZS-TENG at the actual equilibrium position is larger than that at the designed equilibrium position, on account of the decrease in damping ratio induced by the increase in stiffness.

5. Conclusions

In this paper, a sliding-triboelectric nanogenerator is combined with the quasi-zero-stiffness (QZS) mechanism, to form a quasi-zero-stiffness triboelectric nanogenerator (QZS-TENG) for

effectively converting the low-frequency ambient vibration energy to electrical energy. In order to improve the energy conversion efficiency, the configuration of the QZS-TENG is optimized by replacing the traditional negative stiffness mechanism (NSM) with a QZS spring. The analytical results indicate that the QZS spring can produce quite a large displacement region of low stiffness, which is useful to fulfil ultra-low frequency vibration energy harvesting. The dynamic features of the QZS-TENG are determined by the harmonic balance method, to allow evaluation of the energy harvesting efficiency.

Considering the actual expression of the restoring force and the load resistance, the coupled dynamics equation and the electrical equation are established. Then, the numerical results are obtained by solving the coupled equations, which show excellent agreement with the theoretical ones. The analytical and numerical results show that the proposed QZS-TENG has an excellent energy harvesting performance in a very low-frequency region (<4 Hz). In addition, the optimal load resistance is founded by the numerical analysis, which makes the QZS-TENG output the maximal power (>6 mW). The effect of the excitation amplitude and the stiffness ratio on the energy harvesting performance are also discussed. This work provides a novel way to effectively harvest the ambient vibration energy in a very low-frequency region by using the QZS-TENG, which has potential application in powering wireless sensors continuously.

Acknowledgments

This research work was supported by China Postdoctoral Science Foundation (2020M672476), National Natural Science Foundation of China (12002122, 11972152) and National Key R&D Program of China (2017YFB1102801). The first author, Kai Wang, would like to thank the support from the China Scholarship Council (CSC) which sponsors his visit to the University of Liverpool, where the idea of this energy harvester was conceptualised.

References

[1] J. Falnes, A review of wave-energy extraction, Mar. Struct. 20 (2007) 185–201. doi:10.1016/j.marstruc.2007.09.001.

[2] S. Naifar, S. Bradai, C. Viehweger, O. Kanoun, Survey of electromagnetic and magnetoelectric vibration energy harvesters for low frequency excitation, Measurement. 106 (2017) 251–263. doi:10.1016/j.measurement.2016.07.074.

[3] D. Zhu, M.J. Tudor, S.P. Beeby, A tunable kinetic energy harvester with dynamic over range protection, Smart Mater. Struct. 19 (2010) 115005. doi:10.1088/0964-1726/19/11/115005.

[4] M.A. Halim, R. Rantz, Q. Zhang, L. Gu, K. Yang, S. Roundy, An electromagnetic rotational energy harvester using sprung eccentric rotor , driven by pseudo-walking motion, Appl. Energy. 217 (2018) 66–74. doi:10.1016/j.apenergy.2018.02.093.

[5] F. Muhammad, C. Ket, L. Ooi, D. Yurchenko, Increased power output of an electromagnetic vibration energy harvester through anti-phase resonance, Mech. Syst. Signal Process. 116 (2019) 129–145. doi:10.1016/j.ymssp.2018.06.012.

[6] H. Zhang, L.R. Corr, T. Ma, Effects of electrical loads containing non-resistive components on electromagnetic vibration energy harvester performance, Mech. Syst. Signal Process. 101 (2018) 55–66. doi:10.1016/j.ymssp.2017.08.031.

[7] A.G.A. Bernal, L.E.L. Garc á, The modelling of an electromagnetic energy harvesting architecture, Appl. Math. Model. 36 (2012) 4728–4741. doi:10.1016/j.apm.2011.12.007.

[8] S. Mohammadi, A. Esfandiari, Magnetostrictive vibration energy harvesting using strain energy method, Energy. 81 (2015) 519–525. doi:10.1016/j.energy.2014.12.065.

[9] Z.L. Wang, On Maxwell ' s displacement current for energy and sensors : the origin of nanogenerators, Biochem. Pharmacol. 20 (2017) 74–82. doi:10.1016/j.mattod.2016.12.001.

[10] Q. Deng, M. Kammoun, A. Erturk, P. Sharma, Nanoscale flexoelectric energy harvesting À Di v, Int. J. Solids Struct. 51 (2014) 3218–3225. doi:10.1016/j.ijsolstr.2014.05.018.

[11] L. Guo, Q. Lu, Numerical analysis of a new piezoelectric-based energy harvesting pavement system : Lessons from laboratory-based and fi eld-based simulations, Appl. Energy. 235 (2019) 963–977. doi:10.1016/j.apenergy.2018.11.037.

[12] W. He, Y. Qian, B.S. Lee, F. Zhang, A. Rasheed, J. Jung, D.J. Kang, Ultrahigh Output Piezoelectric and Triboelectric Hybrid Nanogenerators Based on ZnO Nano fl akes / Polydimethylsiloxane Composite Films, ACS Appl. Mater. Interfaces. 10 (2018) 44415–44420. doi:10.1021/acsami.8b15410.

[13] X. Shan, H. Li, Y. Yang, J. Feng, Y. Wang, T. Xie, Enhancing the performance of an underwater piezoelectric energy harvester based on fl ow-induced vibration, Energy. 172 (2019) 134–140. doi:10.1016/j.energy.2019.01.120.

[14] Y. Amini, M. Heshmati, P. Fatehi, S.E. Habibi, Piezoelectric energy harvesting from vibrations of a beam subjected to multi-moving loads, Appl. Math. Model. 49 (2017) 1–16. doi:10.1016/j.apm.2017.04.043.

[15] J. Siang, M.H. Lim, M.S. Leong, Review of vibration - based energy harvesting technology : Mechanism and architectural approach, Int. J. Energy Res. 42 (2018) 1866–1893. doi:10.1002/er.3986.

[16] Y. Zhu, H. Wang, D. Zhao, J. Zhao, Energy conversion analysis and performance research on a cone-type dielectric electroactive polymer generator, Smart Mater. Struct. 20 (2011) 115022. doi:10.1088/0964-1726/20/11/115022.

[17] Z.H. Lai, G. Thomson, D. Yurchenko, D. V. Val, E. Rodgers, On energy harvesting from a vibro-impact oscillator with dielectric membranes, Mech. Syst. Signal Process. 107 (2018) 105–121. doi:10.1016/j.ymssp.2018.01.025.

[18] M. Ma, Z. Kang, Q. Liao, Q. Zhang, F. Gao, X. Zhao, Z. Zhang, Development , applications , and future directions of triboelectric nanogenerators, Nano Res. 1 (2018) 1–19.

[19] W. Kim, D. Bhatia, S. Jeong, D. Choi, Mechanical energy conversion systems for triboelectric nanogenerators : Kinematic and vibrational designs, Nano Energy. 56 (2019) 307–321. doi:10.1016/j.nanoen.2018.11.056.

[20] S. Niu, S. Wang, L. Lin, Y. Liu, S. Zhou, Z. Lin, Theoretical study of contact-mode triboelectric nanogenerators as an effective power source, Energy&Environmental Sci. 6 (2013) 3576–3583. doi:10.1039/c3ee42571a.

[21] R. Hinchet, A. Gha, Y. Lu, J.Y. Hasani, S. Kim, P. Basset, Understanding and modeling of triboelectric-electret nanogenerator, Nano Energy. 47 (2018) 401–409. doi:10.1016/j.nanoen.2018.02.030.

[22] D. Bhatia, W. Kim, S. Lee, S. Woo, D. Choi, Tandem triboelectric nanogenerators for optimally scavenging mechanical energy with broadband vibration frequencies, Nano Energy. 33 (2017) 515–521. doi:10.1016/j.nanoen.2017.01.059.

[23] C. Zhai, X. Chou, J. He, L. Song, Z. Zhang, T. Wen, Z. Tian, An electrostatic discharge based needle-to-needle booster for dramatic performance enhancement of triboelectric nanogenerators, Appl. Energy. 231 (2018) 1346–1353. doi:10.1016/j.apenergy.2018.09.120.

[24] Y. Fu, H. Ouyang, R.B. Davis, Nonlinear dynamics and triboelectric energy harvesting from a three-degree-of-freedom vibro-impact oscillator, Nonlinear Dyn. 92 (2018) 1985–2004.

[25] Y. Fu, H. Ouyang, R.B. Davis, Triboelectric energy harvesting from the vibro-impact of three cantilevered beams, Mech. Syst. Signal Process. 121 (2019) 509–531. doi:10.1016/j.ymssp.2018.11.043.

[26] Y. Fu, H. Ouyang, R.B. Davis, Effects of electrical properties on vibrations via electromechanical coupling in triboelectric energy harvesting, J. Phys. D. Appl. Phys. 53 (2020) 215501. doi:10.1088/1361-6463/ab7792.

[27] S. Niu, Y. Liu, S. Wang, L. Lin, Y.S. Zhou, Y. Hu, Z.L. Wang, Theory of Sliding-Mode Triboelectric Nanogenerators, Adv. Mater. 25 (2013) 6184–6193. doi:10.1002/adma.201302808.

[28] C. Zhang, W. Tang, C. Han, F. Fan, Z.L. Wang, Theoretical Comparison , Equivalent Transformation , and Conjunction Operations of Electromagnetic Induction Generator and Triboelectric Nanogenerator for Harvesting Mechanical Energy, Adv. Mater. (2014) 3580–3591. doi:10.1002/adma.201400207.

[29] C. Zhang, W. Tang, Y. Pang, C. Han, Z.L. Wang, Active Micro-Actuators for Optical Modulation Based on a Planar Sliding Triboelectric Nanogenerator, Adv. Mater. 27 (2015) 719–726. doi:10.1002/adma.201404291.

[30] Y. Fu, H. Ouyang, R. Benjamin Davis, Nonlinear structural dynamics of a new sliding-mode triboelectric energy harvester with multistability, Nonlinear Dyn. 100 (2020) 1941–1962. doi:10.1007/s11071-020-05645-z.

[31] S. Wang, Y. Xie, S. Niu, L. Lin, Z.L. Wang, Freestanding Triboelectric-Layer-Based Nanogenerators for Harvesting Energy from a Moving Object or Human Motion in Contact and Non-contact Modes, Adv. Mater. 26 (2014) 2818–2824. doi:10.1002/adma.201305303.

[32] S. Wang, S. Niu, J. Yang, L. Lin, Z.L. Wang, W.E.T. Al, Quantitative Measurements of Vibration Amplitude Using a Contact-Mode Freestanding Triboelectric Nanogenerator, ACS Nano. 8 (2014) 12004–12013. doi:10.1021/nn5054365.

[33] F. Fan, Z. Tian, Z. Lin, Flexible triboelectric generator !, Nano Energy. 1 (2012) 328–334. doi:10.1016/j.nanoen.2012.01.004.

[34] P. Bai, G. Zhu, Q. Jing, Y. Wu, J. Yang, Transparent and fl exible barcode based on sliding electri fi cation for self-powered identi fi cation systems, Nano Energy. 12 (2015) 278–286. doi:10.1016/j.nanoen.2015.01.005.

[35] Y. Yang, H. Zhang, Z. Lin, Y.S. Zhou, Q. Jing, Y. Su, J. Yang, Human Skin Based Triboelectric Nanogenerators for Harvesting Biomechanical Energy and as Self-, ACS Nano. 7 (2013) 9213–9222. doi:10.1021/nn403838y.

[36] J. Yang, J. Chen, Y. Yang, H. Zhang, W. Yang, P. Bai, Y. Su, Z.L. Wang, Broadband Vibrational Energy Harvesting Based on a Triboelectric Nanogenerator, Adv. Mater. 4 (2014) 1301322. doi:10.1002/aenm.201301322.

[37] C. Wu, R. Liu, J. Wang, Y. Zi, L. Lin, Z. Lin, A spring-based resonance coupling for hugely enhancing the performance of triboelectric nanogenerators for harvesting low-frequency vibration energy, Nano Energy. 32 (2017) 287–293. doi:10.1016/j.nanoen.2016.12.061.

[38] X. He, Q. Wen, Y. Sun, Z. Wen, A low-frequency piezoelectric-electromagnetic-triboelectric hybrid broadband

vibration energy harvester, Nano Energy. 40 (2017) 300–307. doi:10.1016/j.nanoen.2017.08.024.

[39] M. Salauddin, R.M. Toyabur, P. Maharjan, J.Y. Park, High performance human-induced vibration driven hybrid energy harvester for powering portable electronics, Nano Energy. 45 (2018) 236–246. doi:10.1016/j.nanoen.2017.12.046.

[40] Y. Yang, H. Zhang, J. Chen, Q. Jing, Y.S. Zhou, X. Wen, Z.L. Wang, Single-Electrode-Based Sliding Triboelectric Nanogenerator for Self-Powered Displacement, ACS Nano. 7 (2013) 7342–7351.

[41] J. Zhou, K. Wang, D. Xu, H. Ouyang, Local resonator with high-static-low-dynamic stiffness for lowering band gaps of flexural wave in beams, J. Appl. Phys. 121 (2017) 044902. doi:http://dx.doi.org/10.1063/1.4974299.

[42] K. Wang, J. Zhou, D. Xu, Sensitivity analysis of parametric errors on the performance of a torsion quasi-zero-stiffness vibration isolator, Int. J. Mech. Sci. 134 (2017) 336–346. doi:10.1016/j.ijmecsci.2017.10.026.

[43] X. Sun, X. Jing, Multi-direction vibration isolation with quasi-zero stiffness by employing geometrical nonlinearity, Mech. Syst. Signal Process. 62 (2015) 149–163. doi:10.1016/j.ymssp.2015.01.026.

[44] Z. Hao, Q. Cao, M. Wiercigroch, Nonlinear dynamics of the quasi-zero-stiffness SD oscillator based upon the local and global bifurcation analyses, Nonlinear Dyn. 87 (2017) 987–1014. doi:10.1007/s11071-016-3093-6.

[45] K. Wang, J. Zhou, Y. Chang, H. Ouyang, D. Xu, Y. Yang, A nonlinear ultra-low-frequency vibration isolator with dual quasi-zero-stiffness mechanism, Nonlinear Dyn. 101 (2020) 755–773. doi:10.1007/s11071-020-05806-0.

[46] S. Wang, L. Lin, Y. Xie, Q. Jing, S. Niu, Z.L. Wang, Sliding-Triboelectric Nanogenerators Based on In-Plane Charge- Separation Mechanism, Nano Lett. 13 (2013) 2226–2233.

[47] K. Wang, J. Zhou, H. Ouyang, L. Cheng, D. Xu, A semi-active metamaterial beam with electromagnetic quasi-zero-stiffness resonators for ultralow-frequency band gap tuning, Int. J. Mech. Sci. 176 (2020) 105548. doi:10.1016/j.ijmecsci.2020.105548.

[48] S. Niu, Z. Lin, Theoretical systems of triboelectric nanogenerators, Nano Energy. 14 (2015) 161–192. doi:10.1016/j.nanoen.2014.11.034.